

3D spatio-kinematic modeling of Abell 48, a planetary nebula around a Wolf-Rayet [WN] star[★]

A. Danehkar^{1†}

¹*Department of Astronomy, University of Michigan, 1085 S. University Ave., Ann Arbor, MI 48109, USA*

23 December 2021

ABSTRACT

The planetary nebula (PN) Abell 48 (NGC 029.0+00.4) is around a rare Wolf-Rayet [WN5] star whose stellar history is as yet unknown. Using the integral field observations of the H α λ 6563 and [N II] λ 6584 line emissions, we conducted a comprehensive spatio-kinematic analysis of this PN. A three-dimensional spatio-kinematic ionization model was developed with the kinematic modeling tool SHAPE to replicate the observed spatially-resolved velocity channels and position–velocity diagrams. According to our kinematic analysis of the H α emission, this object possesses a deformed elliptic toroidal shell with an outer radius of 23 arcsec and a thickness of 15 arcsec associated with an integrated H α emission-line expansion of $\sim 35 \pm 5$ km s^{−1}, a maximum poloidal expansion of around 70 ± 20 km s^{−1} at an inclination angle of $\sim 30^\circ$ with respect to the line of sight, and a position angle of $\sim 130^\circ$ measured from east toward north in the equatorial coordinate system. Furthermore, [N II] kinematic modeling reveals the presence of narrow (~ 3 arcsec) exterior low-ionization structures surrounding the main elliptical shell, which could have formed as a result of shock collisions with the interstellar medium. The torus-shaped morphology of this PN could be related to its unusual hydrogen-deficient [WN] nucleus that needs to be inspected further.

Key words: planetary nebulae: individual: PN Abell 48 — ISM: kinematics and dynamics — stars: Wolf–Rayet.

1 INTRODUCTION

Abell 48 (= NGC 029.0+00.4 = A66 48 = PK 029+00 1) was detected and classified as a planetary nebula (PN) by Abell (1955). Its ring-shaped morphology was first seen in the photographic images collected for the Palomar Observatory Sky Survey (Abell 1966). Kromov & Kohoutek (1968) described its morphology as a ring-like shape with a mean angular diameter of $40''$ using images prepared for the Catalogue of Galactic Planetary Nebulae (Perek & Kohoutek 1967). In the H α survey of PNe with the Palomar 1.5 m telescope, Jewitt et al. (1986) identified its morphological class as a ring-type without any halo. The boundaries of this PN correspond to angular dimensions of $46'' \times 38''$, i.e., a maximum radius of $23''$ and a shell thickness of around $15''$ when seen at roughly 10 percent of its mean surface brightness in the H α band of the SuperCOSMOS H α Sky Survey (SHS; Parker et al. 2005).

The central star of Abell 48 has caused some controversies (Wachter et al. 2010; Todt et al. 2013; Frew et al. 2014). Previously, Zuckerman & Aller (1986) described its stellar characteristics as [WC] with O VI. We use the square brackets to separate the Wolf-Rayet (WR) central stars of planetary nebulae from their massive WR counterparts. However, Wachter et al. (2010) classified it as a massive WN6 with a ring nebula. DePew et al. (2011) also suggested that it may be either [WN] or [WN/WC] surrounded by a PN similar to the PN PB 8 with a [WN/WC] star (Todt et al. 2010), and IC 4663 with a [WN] star (Miszalski et al. 2012). Detailed

spectral analyses of the central star of Abell 48 pointed to either [WN5] (Todt et al. 2013) or [WN5-6] (Frew et al. 2014) instead of a massive WN6 (Pop I) star. More recently, a comparison between the H II λ 4686 lines emitted by the Abell 48 central star and the WN7 star of WR 148 exhibits an asymmetric profile toward the red wing in WR 148, whereas we see a rather symmetric profile in Abell 48 that could be a signature of a lower mass-loss rate associated with a low-mass [WR] star (Munoz et al. 2017).

The oxygen abundance of the PN Abell 48 was reported to be $O/H = 1.6 \times 10^{-4}$ (Danehkar et al. 2014) and 2.7×10^{-4} (Todt et al. 2013). Its low metallicity may help to form its [WR] central star (Zijlstra et al. 2006; Kniazev et al. 2008; Miller Bertolami et al. 2011). A self-consistent photoionization model of this object constructed by Danehkar et al. (2014) also reproduced its nebular spectrum with a low metallicity ($O/H = 1.4 \times 10^{-4}$) at a distance of 1.9 kpc using the hydrogen-deficient expanding model constrained by Todt et al. (2013) as its ionizing source. However, a solar metallicity ($O/H = 4.9 \times 10^{-4}$) was also derived by adopting different physical conditions (Frew et al. 2014), which may not lead to a [WN] star. We should note that electron densities of ~ 750 (Danehkar et al. 2014; Frew et al. 2014) and 1000 cm^{−3} (Todt et al. 2013) were also determined from the [S II] line ratio. Moreover, an electron temperature of around 7000 K was also deduced from the [N II] line ratio (Todt et al. 2013; Danehkar et al. 2014; Frew et al. 2014). Although the [O III] λ 4363 auroral line is extremely faint, higher uncertain temperatures of $\lesssim 9950$ K (Frew et al. 2014) and 11900 K (Todt et al. 2013) were also calculated using the [O III] $\lambda\lambda$ 4959,5007/ λ 4363 ratio. The accuracy of chemical abundances largely depends on the electron temperature assumed for empirical

[★] Based on observations with the Australian National University 2.3-m Advanced Technology Telescope under program 1100147.

[†] E-mail: danehkar@umich.edu

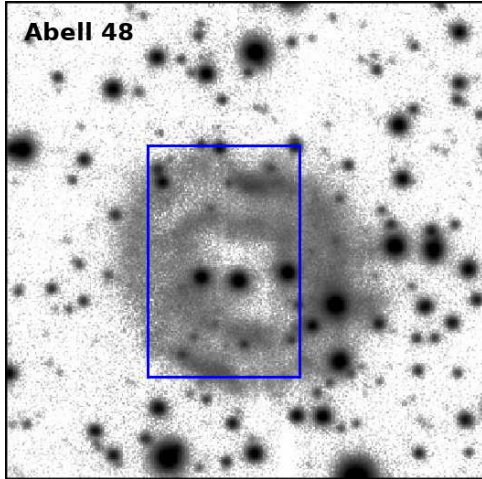


Figure 1. The r_{P1} -band image of Abell 48 from the PS1 survey (Chambers et al. 2016; Flewelling et al. 2020). The rectangle corresponds to the IFU FOV ($25'' \times 38''$) of the WiFeS taken in 2010 April. The image is oriented with north up and east to the left.

abundance analysis (see e.g. Danehkar 2021b), so this PN could have a metallicity ranging from sub-solar to solar composition.

In this work, we employ integral field spatially resolved kinematic maps and position-velocity (P-V) arrays of the PN Abell 48 to build a three-dimensional (3D) kinematic model of this object. In Section 2, we briefly describe the observation. The kinematic observations are present in Section 3, followed by a spatio-kinematic model in Section 4. Our conclusion is drawn in Section 5.

2 OBSERVATION

The moderate-resolution kinematic observation of the PN Abell 48 studied in this work was collected on April 22, 2010 with the Wide Field Spectrograph (WiFeS; Dopita et al. 2007, 2010), on the 2.3-m telescope operated by the Australian National University (program number 1100147, PI: Q.A. Parker). The WiFeS is a double-beam integral field unit (IFU) spectrograph with a field-of-view (FOV) of $25'' \times 38''$, a spatial resolution of $1''.0 \times 0''.5$, and a full width at half-maximum of the reconstructed point-spread function (PSF) of approximately $2''$ on 4096×4096 -pixel CCD detectors. Volume phase holographic gratings utilized by the WiFeS yield spectral resolutions of $R \sim 3000$ and $R \sim 7000$. The observation was taken with an exposure time of 1200 sec, while the WiFeS grating was configured to $R \sim 7000$ that leads a linear wavelength dispersion per pixel of 0.45 \AA in the red arm over $\lambda\lambda 5222\text{--}7070 \text{ \AA}$, resulting in a velocity channel resolution of around 21 km s^{-1} .

The IRAF pipeline *wifes* was used to perform the standard data reduction (fully described in Danehkar et al. 2014; Danehkar 2021a). This procedure includes averaged bias subtraction, pixel-to-pixel sensitivity correction using flat-field frames, spectral calibration with Cu-Ar arc lamp exposures, spatial calibration using wire frames, atmospheric refraction correction, cosmic ray removal, and flux calibration.

Figure 1 shows the r_{P1} -band image ($\lambda_{\text{mean}} = 6215 \text{ \AA}$ and $\Delta\lambda \approx 1600 \text{ \AA}$) of Abell 48 in the Pan-STARRS1 (PS1) survey (Chambers et al. 2016; Flewelling et al. 2020) that was retrieved from the Mikulski Archive for Space Telescopes (MAST). The

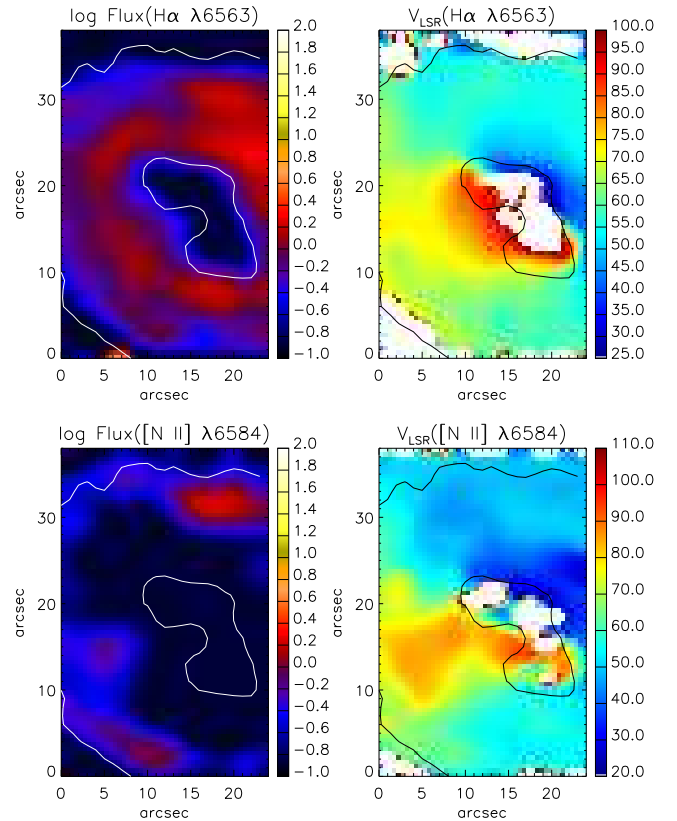


Figure 2. IFU maps of Abell 48 in the $H\alpha \lambda 6563 \text{ \AA}$ (top panels) and $[N \text{ II}] \lambda 6584 \text{ \AA}$ (bottom). From left to right, the logarithmic flux map in $10^{-15} \text{ erg s}^{-1} \text{ cm}^{-2} \text{ spaxel}^{-1}$ unit, and LSR radial velocity map in km s^{-1} . The contours correspond to ~ 10 percent of the mean $H\alpha$ surface brightness of this object seen in the SHS. The field is oriented with north up and east to the left.

rectangle on the PS1 image depicts the WiFeS areal footprint used for the 2010 observation.

3 KINEMATIC RESULTS

Figure 2 presents the spatially resolved maps of the flux intensity and radial velocity of Abell 48 for the $H\alpha \lambda 6563$ and $[N \text{ II}] \lambda 6584$ emission seen in the WiFeS field. The velocity map is in the local standard of rest (LSR) and was transferred using the IDL implementation (written by D. Nidever, 2006) of the IRAF task *rvcorrect*. The white/black contours in the figures correspond to about 10 percent of the SuperCOSMOS $H\alpha$ Sky Survey (SHS; Parker et al. 2005) mean surface brightness of this PN. It can be seen that the IFU maps illustrate an inclined ring-shaped nebula.

We obtained an expansion velocity of $35 \pm 5 \text{ km s}^{-1}$ that corresponds to the half width at half maximum (HWHM) measurement of the $H\alpha \lambda 6563$ emission line in the integrated spectrum extracted from the entire nebula covered by the WiFeS FOV. The systemic velocity measured from the $H\alpha \lambda 6563$ emission line was found to be $v_{\text{sys}} = 65 \pm 5 \text{ km s}^{-1}$ in the LSR, which agrees with the previous results (Todt et al. 2013; Danehkar et al. 2014). The P-V array and velocity channel maps in the $H\alpha$ emission also point to $v_{\text{sys}} = 62 \text{ km s}^{-1}$, albeit with a velocity resolution of about 21 km s^{-1} . The systemic velocity estimated from the emission-line

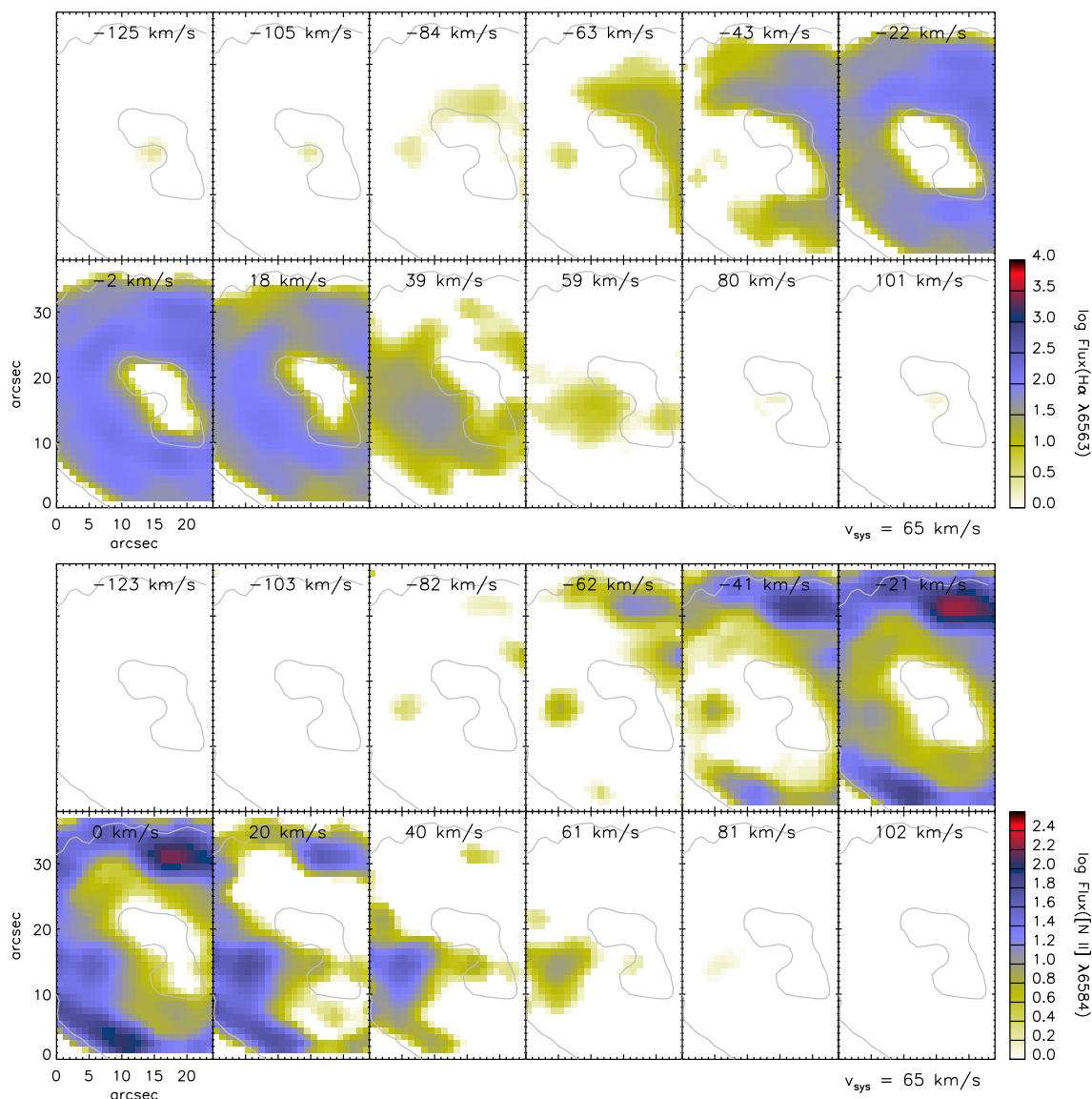


Figure 3. Velocity slices of Abell 48 along the $\text{H}\alpha$ $\lambda 6563$ Å (top panels) and $[\text{N II}]$ $\lambda 6584$ Å (bottom) emission with central velocities in km s^{-1} at the top. The velocity width of each slice is around 21 km s^{-1} . The systemic velocity is $v_{\text{sys}} = 65 \text{ km s}^{-1}$ in the LSR frame. The color bars correspond to the logarithmic fluxes in $10^{-15} \text{ erg s}^{-1} \text{ cm}^{-2} \text{ spaxel}^{-1}$. The gray contours are associated with ~ 10 percent of the mean surface brightness of this PN seen in the SHS. The field is oriented with north up and east to the left.

profile integrated over all the spaxels of the entire nebula seems to be more accurate than the P–V diagram and velocity channels with a slice interval of $\sim 21 \text{ km s}^{-1}$.

Figure 3 presents the logarithmic flux distributions of the $\text{H}\alpha$ and $[\text{N II}]$ emissions in a series of 12 velocity channel maps with a width of about 21 km s^{-1} that span from -125 to 102 km s^{-1} . The stellar continua were determined and subtracted from them. The central velocity is also provided at the top of each channel, which is relative to the systemic velocity $v_{\text{sys}} = 65 \text{ km s}^{-1}$. The $\text{H}\alpha$ velocity channel maps show different components in the -43 , -22 , -2 , 18 , 39 km s^{-1} velocities, which are associated with the front and rear ends of a toroidal shell expanding at $\sim 35 \pm 5 \text{ km s}^{-1}$ with respect to the central star. Similarly, the $[\text{N II}]$ channel maps suggest the same expanding velocity, but with a high distribution of N^+ towards the outer boundary of the nebula. However, the outer radius of the nebula in the $[\text{N II}]$ emission is about 3 arcsec larger

than that in the $\text{H}\alpha$ emission, which could suggest the presence of a narrow, low-ionization N^+ layer surrounding the photoionized H^+ main shell. Assuming that this nebula is a circle-shaped ring inclined at an angle ($i = 30^\circ$, see § 4) projected on the sky plane, the symmetric axis of this object has a position angle (PA) of $130^\circ \pm 2^\circ$ from the direction of the north towards the east in the equatorial coordinate system (ECS).

Figure 4 (top panels) presents the P–V diagrams in the $\text{H}\alpha$ $\lambda 6563$ (right) and $[\text{N II}]$ $\lambda 6584$ emission (left) produced from the IFU datacube for two slits positioned through the central star and oriented with $\text{PA} = 130^\circ$ of the symmetric axis and 40° perpendicular to the symmetric axis. The velocity axes are relative to the systemic velocity ($v_{\text{sys}} = 65 \text{ km s}^{-1}$). The central star is located at 0 arcsec in the angular axes. The stellar continua were also determined and removed from the P–V diagrams. The two separate knots seen in the $\text{H}\alpha$ P–V diagrams are the front and rear

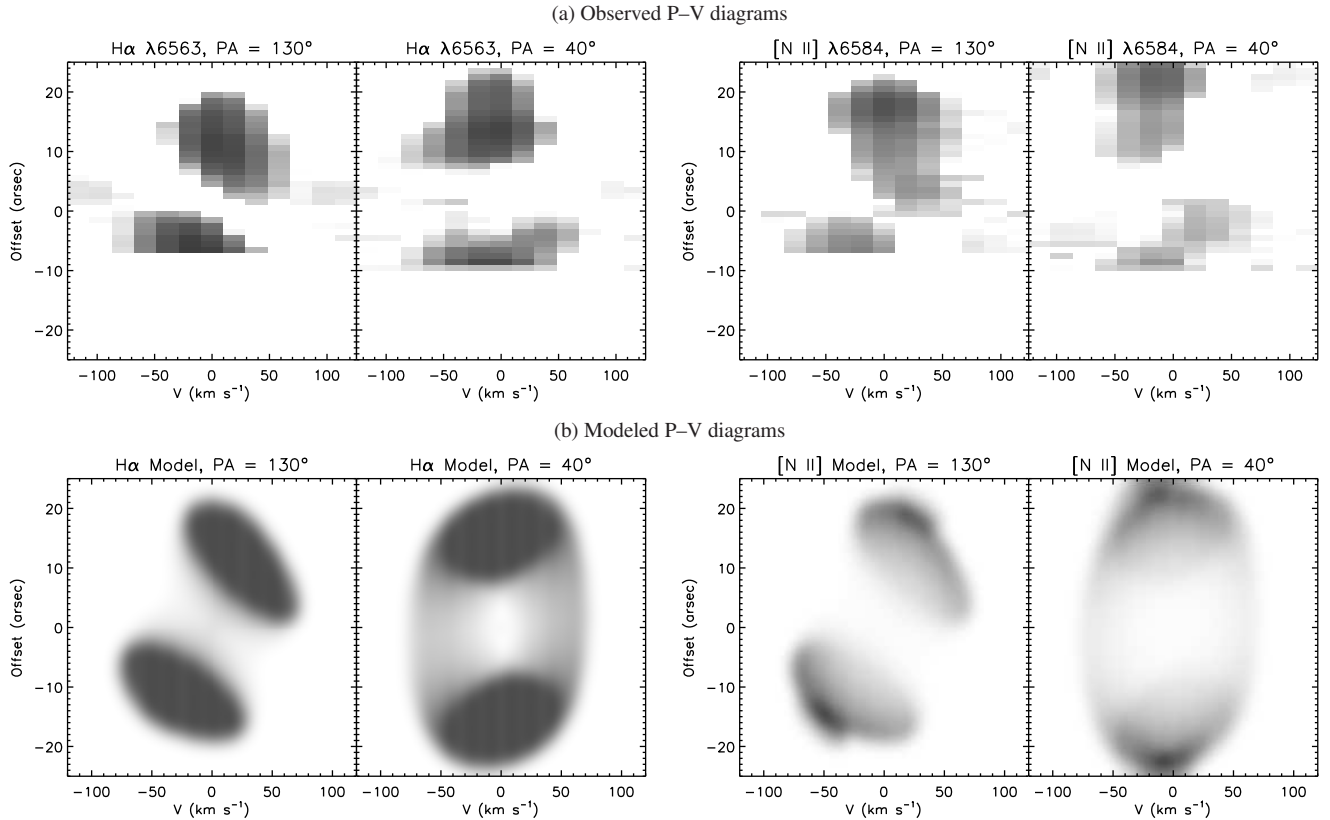


Figure 4. *Top Panels:* Observed P–V diagrams of Abell 48 in the $H\alpha$ $\lambda 6563$ (right panels) and $[N\text{ II}]$ $\lambda 6584$ emission (left). Slits are oriented with $PA = 130^\circ$ and 40° through the central star. The velocity axis is given in km s^{-1} relative to the systemic velocity of the PN. The angular offset at 0 arcsec corresponds to the central star. *Bottom Panels:* The associated synthetic P–V arrays rendered from the spatio-kinematic model with density laws describing the $H\alpha$ $\lambda 6563$ (right panels) and $[N\text{ II}]$ $\lambda 6584$ (left) observations of Abell 48.

parts of a projected torus. It can be seen that the top and bottom sides of the toroidal shell reach a deprojected poloidal velocity of $v_{\text{pol-exp}} = 70 \pm 20 \text{ km s}^{-1}$ with respect to the central center. As can be seen, the IFU footprint did not fully capture the lower portion of the P–V arrays. Again, similar to the velocity channels, the nebular size seen in the $[N\text{ II}]$ P–V array at $PA = 40^\circ$ is slightly larger than what we see in the $H\alpha$ diagram, implying the existence of an exterior low-ionization structure beyond the photoionized H^+ region. This low-ionization N^+ zone could be produced by the interaction with the interstellar medium (ISM).

4 SPATIO-KINEMATIC MODELING

To reproduce spatially resolved kinematic maps and P–V arrays, we have employed the kinematic modeling tool SHAPE v5.0 (Steffen & López 2006; Steffen et al. 2011). This tool allows us to interactively create and modify 3D geometries using polygon meshes, and to define velocity and density laws for 3D geometries. It applies a ray-casting algorithm to volumic grids of defined 3D geometries to produce radiative transfer solutions through them, resulting in synthetic images, P–V diagrams, and velocity channels. To find the best-fitting model, it is necessary to iteratively adjust 3D geometries, velocity and density laws, orientation and inclination angles until we get solutions that closely resemble observations. 3D geometries can also be exported from the SHAPE platform to 3D models in the standard triangle language (STL) file format

that can also be transformed into other appropriate file formats such as the Alias/WaveFront object file format using a mesh processing program such as MeshLab (Cignoni et al. 2008) for online publication. This modeling tool has been employed to construct 3D kinematic models of several PNe, such as NGC 2392 (García-Díaz et al. 2012), Hb 5 and K 3-17 (López et al. 2012), Th 2-A (Danehkar 2015), Abell 14 (Akras et al. 2016), and Hb 4 (Derlopa et al. 2019).

Figure 5 (left) depicts the kinematic wireframe model of Abell 48 at three different views (top: $i = 0^\circ$, front and side: 90°), as well as their best-fitting inclination ($i = 30^\circ$) and orientation ($PA = 130^\circ$) that well reproduce the IFU observations, followed by the two rendered images associated with two different density laws for the $H\alpha$ and $[N\text{ II}]$ emissions, respectively. The 3D model is also provided in the Alias/WaveFront object file format on Sketchfab with a representative image in Figure 5 (right), and archived on Zenodo.¹ The mesh model reproducing the $H\alpha$ emission is built of a torus that is deformed using the size, shear, and squish modifiers in the SHAPE platform. The *size* modifier transforms it into an elliptic torus by stretching it by a factor of 2 along the z axis. Additionally, this elliptic torus is also surrounded by an exterior elliptic torus that reproduces the observed P–V array in the $[N\text{ II}]$ emission, but the outer torus is deactivated for the $H\alpha$ kinematic model via the density function. This kinematic model helps to

¹ <https://doi.org/10.5281/zenodo.5511247>

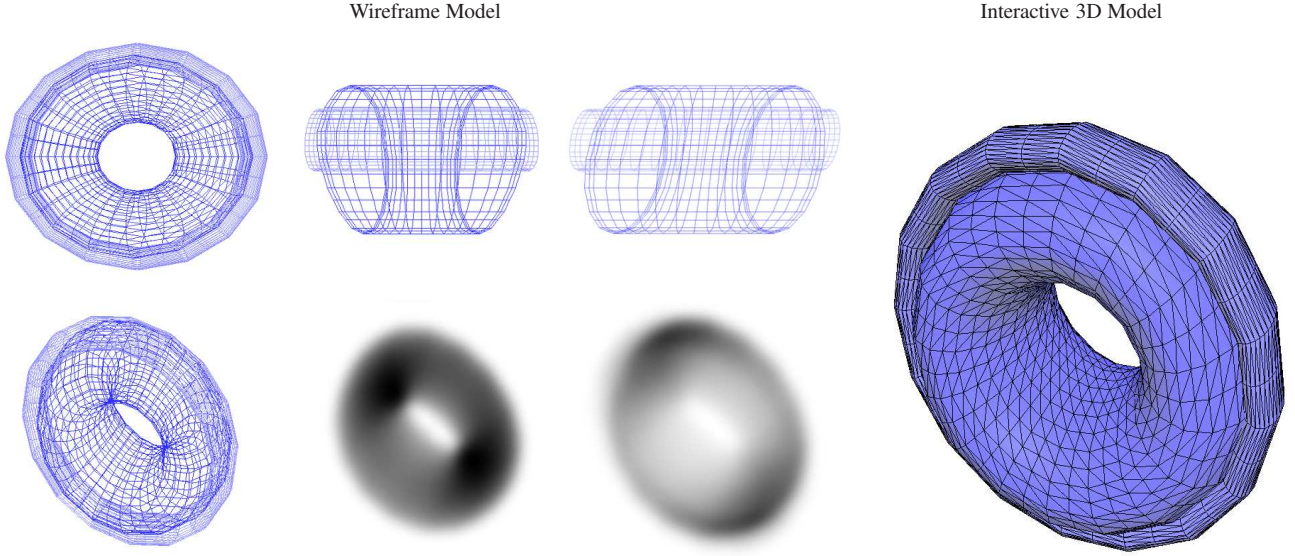


Figure 5. *Left Panel:* Spatio-kinematic wireframe model of Abell 48 seen from the top view ($i = 0^\circ$), the front and side view ($i = 90^\circ$), and the best-fitting inclination ($i = 30^\circ$) and orientation (PA = 130°), followed by the rendered images for the H α $\lambda 6563$ and [N II] $\lambda 6584$ emissions made with two different density laws, respectively. The exterior elliptic torus is used only for modeling the [N II] emission. *Right Panel:* Interactive 3D model available on Sketchfab (<https://skfb.ly/o7nxA>) for the online journal.

reproduce a maximum poloidal velocity of $v_{\text{pol-exp}} = 70 \text{ km s}^{-1}$ with respect to the center, while the elliptic toroidal shell expands with an averaged integrated H α emission-line velocity of $v_{\text{HWHM}} = 35 \text{ km s}^{-1}$. Moreover, the *shear* operator pushes the geometry by misaligned pressure in the x direction, which reproduces the pattern seen in the observed P–V array along the minor axis (PA = 40°). Similarly, Jones et al. (2010) applied the shear modifier to an elliptical geometry to emulate the asymmetric morphology of Abell 41. We also utilize the *squish* operator to make a slightly asymmetric elliptic torus whose front side is slightly wider than its rear, resulting in a better match with the observed P–V arrays.

The deformation in the nebular shell could be created by the ISM interaction. Moreover, the exterior narrow N $^+$ layer around the main H $^+$ shell in Abell 48 could also be owing to shock-ionization with the ISM. Similarly, a deformed ring is visible in the PN Hb 4 (Danehkar 2021a) that could be produced as the PN moves through the ISM. Moreover, the PN M 2-42 was found to have a pair of asymmetric bipolar outflows (Danehkar et al. 2016) that could be a sign of the ISM interaction (e.g. Wareing et al. 2007). The possibility of the ISM interaction was also considered for the PN Abell 41 (Jones et al. 2010), for which asymmetric brightness and shape are found. It is worthwhile mentioning that a later outburst from the post-AGB star may also contribute to asymmetric and deformed structures as it pushes away the previously expelled shell, and also results in the formation of low-ionization shocked regions (see e.g. NGC 5189 in Danehkar et al. 2018).

To reproduce the P–V line profiles, a linear radial velocity law is defined as a function of the radial distance $v[\text{km s}^{-1}] = 4 \times r[\text{arcsec}]$. This type of expansion is called the homologous (Hubble-type) velocity law (Steffen et al. 2009). To emulate the IFU observations of the [N II] $\lambda 6584$ emission, we also employ a density law in the main shell that radially increases by a power of 3 outward from the nebular center that closely resembles the N $^+$ ion fraction predicted by the photoionization model (see Figure 7 in Danehkar et al. 2014). Moreover, the outer shell around the main shell is also reproduced the N $^+$ zone in the P–V array at PA = 40°

Table 1. Parameters of the spatio-kinematic model of Abell 48.

Parameter	Value
Inclination of the symmetric axis, i	$30^\circ \pm 2^\circ$
Position angle of the symmetric axis, PA	$130^\circ \pm 2^\circ$
Outer radius of the shell, $r_{\text{out}}(\text{H}\alpha)$	$23 \pm 2 \text{ arcsec}$
Outer radius of the shell, $r_{\text{out}}([\text{N II}])$	$26 \pm 2 \text{ arcsec}$
Thickness of the shell, $\delta r(\text{H}\alpha)$	$15 \pm 2 \text{ arcsec}$
HWHM expansion, $v_{\text{HWHM}}(\text{H}\alpha)$	$35 \pm 5 \text{ km s}^{-1}$
Maximum poloidal expansion, $v_{\text{pol-exp}}$	$70 \pm 20 \text{ km s}^{-1}$
LSR systemic velocity, $v_{\text{sys}}(\text{H}\alpha)$	$65 \pm 5 \text{ km s}^{-1}$

that could be due to shock collisions with the ISM. While we model the H α observations, we deactivate this outer region through the density operator in SHAPE. To improve the [N II] P–V diagrams, we also modify the density profile of the main shell using a sinusoidal expression defined by the polar angle in the spherical coordinate system so that the density decreases as one moves from the equator ($\phi = 90^\circ$) to the poles ($\phi = 0^\circ$ and 180°), with a greater decrease at the south pole ($\phi = 180^\circ$). This inhomogeneous density model is only used for the [N II] observations. Similarly, Akas & López (2012) defined an inhomogeneous density law with thinner polar distributions to recreate the P–V diagrams of BD +30° 3639.

Figure 4 shows a comparison of the synthetic P–V arrays generated by the spatio-kinematic model (bottom panels) with the P–V diagrams observed in H α $\lambda 6563$ and [N II] $\lambda 6584$ (top panels) for two slits oriented along the symmetric axis (PA = 130°) and vertical to the symmetric axis (PA = 40°). As seen in the figure, there are reasonable agreements between the observed and modeled P–V diagrams, while the lower parts of the P–V diagrams were not completely observed by the IFU FOV. Figure 6 also presents the synthetic velocity channels of the model, which can also be compared with the spatially resolved velocity maps

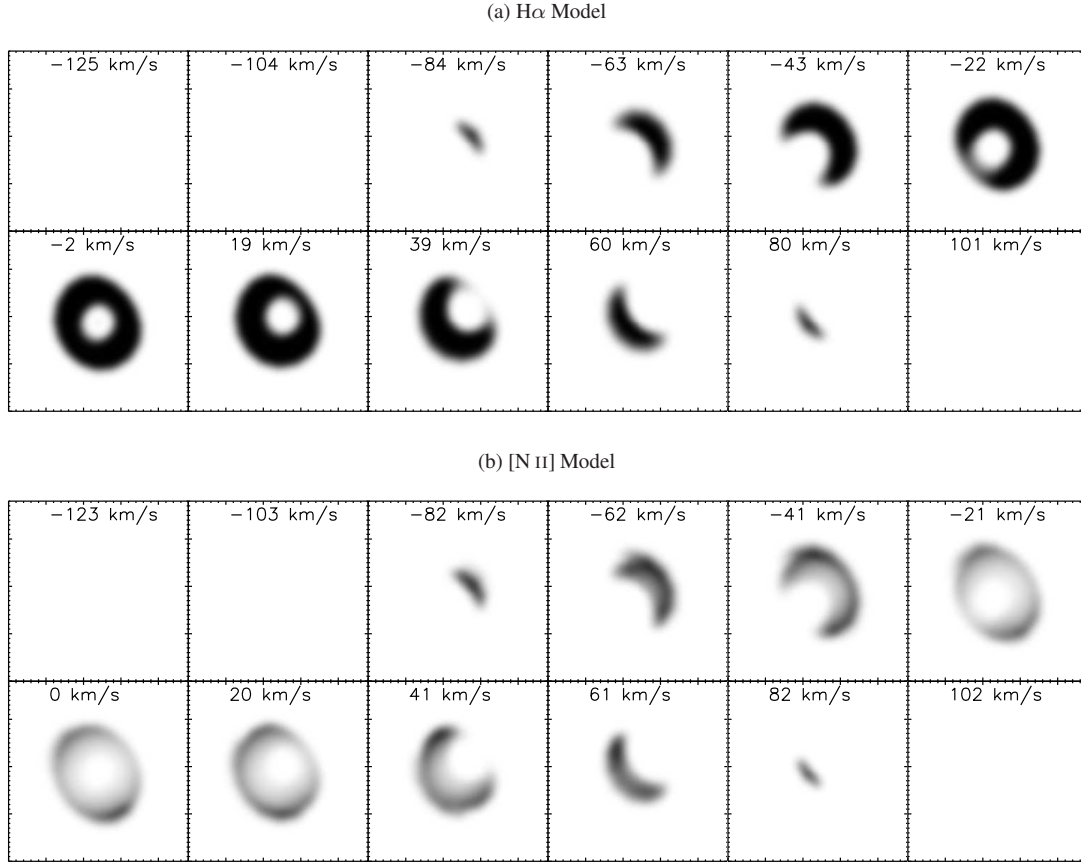


Figure 6. The synthetic velocity channels rendered from the spatio-kinematic model with density laws describing the $H\alpha$ $\lambda 6563$ (top panels) and $[N II]$ $\lambda 6584$ (bottom) observations of Abell 48.

shown in Figure 3. The synthetic results provide a good match to the observed maps, so the model well reproduces the kinematic properties and ionization distributions of the H^+ and N^+ ions in this object. Some discrepancies between the $[N II]$ observations and synthetic P–V arrays are still present, which could be related to asymmetric low-ionization structures (see Figure 2) possibly due to the ISM interaction.

The parameters of the best-fitting models are listed in Table 1. The symmetric axis of this PN has $PA = 130^\circ \pm 2^\circ$ measured from east toward north in the ECS. This PA corresponds to a Galactic position angle of $192.8^\circ.2$ from the north Galactic pole toward the Galactic east. Previously, without any constraints on velocity channel maps and P–V diagrams, a PA of 135° was derived (Danahkar et al. 2014). We also see that the velocity slices and P–V arrays are well matched if the inclination of the major axis is $i = 30^\circ \pm 2^\circ$, whereas $i = 35^\circ \pm 2^\circ$ was found by Danahkar et al. (2014) without detailed kinematic analysis using the older version of SHAPE.² Assuming $D = 1.6 \pm 0.5$ kpc estimated by Frew et al. (2014), the $H\alpha$ outer radius of 23 ± 2 arcsec corresponds to $r_{\text{out}} = 0.178^{+0.074}_{-0.073}$ pc, so the maximum poloidal expansion $v_{\text{pol-exp}} = 70 \pm 20$ km s^{−1} implies a dynamical age of $\tau_{\text{dyn}} = r_{\text{out}}/v_{\text{pol-exp}} = 2490^{+1980}_{-1220}$ yr. As proposed by Dopita et al. (1996), the true age could be $\tau_{\text{true}} = 1.5 \times \tau_{\text{dyn}} = 3740^{+1830}_{-2980}$ yr, in agreement with the

dynamical age of 3900 yr derived by Frew et al. (2014). However, Todt et al. (2013) estimated a nebular age of 6500 yr based on a typical expansion velocity of 30 km s^{−1}. Alternatively, Gesicki & Zijlstra (2000) suggested that the dynamical age should be calculated based on the expansion velocity v_{exp} and the asymptotic giant branch (AGB) velocity $v_{\text{AGB}} = 0.5 \times v_{\text{exp}}$, so the true age of Abell 48 could be $\tau_{\text{true}} = 2r_{\text{out}}/(1.5v_{\text{pol-exp}}) = 3320^{+1620}_{-2650}$ yr. The estimated dynamical ages are consistent with an ionized nebula ejected from an intermediate-mass progenitor star with a final stellar mass of $\lesssim 0.6 M_\odot$. On the other hand, if this nebula is associated with a massive WN star, it should be located at 12 kpc with an ionized mass of $\sim 50 M_\odot$ (Frew et al. 2014). While the expansion velocity could be related to a nebula around a massive WN star, the physical conditions and ionic abundances derived for this nebula are not typical of massive WN nebulae (Todt et al. 2013; Danahkar et al. 2014; Frew et al. 2014).

5 CONCLUSION

Using integral field spectroscopic observations, a comprehensive spatio-kinematic analysis of the PN Abell 48 with a [WN]-type star has been conducted that can reproduce the velocity-resolved channels and P–V arrays observed in the $H\alpha$ $\lambda 6563$ and $[N II]$ $\lambda 6584$ emission line profiles. A 3D spatio-kinematic model has been constructed using a sheared elliptic torus that could be evidence of the PN-ISM interaction that happens as the nebula

² Note that $i = -35^\circ$ reported by Danahkar et al. (2014) using SHAPE v4.5 should be $i = 35^\circ$ with the latest version.

is expanding and moving through the ISM. The extreme poloidal expansion of $v_{\text{pol-exp}} = 70 \pm 20 \text{ km s}^{-1}$ was replicated by velocity components of the stretched, sheared torus in the z direction, while it has a mean integrated $\text{H}\alpha$ emission-line expansion of $v_{\text{HWHM}} = 35 \pm 5 \text{ km s}^{-1}$. The line-of-sight inclination and ECS orientation were found to be $i = 30^\circ \pm 2^\circ$ and $\text{PA} = 130^\circ \pm 2^\circ$, respectively. The [N II] P–V arrays were recreated using an inhomogeneous density profile in the elliptic torus owing to the N^+ ion radial profile produced by the photoionization process (see Danehkar et al. 2014), as well as a thin ($\sim 3 \text{ arcsec}$) external shell likely associated with shock ionization. Some asymmetries seen in the [N II] flux map (Figure 2) could also be related to shock excitation caused by the interaction with the ambient medium.

The central star of Abell 48 has been identified as a [WN]-type star (Todt et al. 2013; Frew et al. 2014). Its hydrogen-deficient stellar characteristics may have emerged when its hydrogen-rich stellar layer was lost to a companion, but we have not yet detected any binary system in this object. We know that some PNe with similar elliptical ring-shaped morphology evolved from common envelopes with binarity, such as Abell 63 (Mitchell et al. 2007), Abell 41 (Jones et al. 2010), Sp 1 (Jones et al. 2012), and HaTr 4 (Tyndall et al. 2012), whose symmetric axes are roughly perpendicular to their binary orbital planes. An in-depth monitoring of its central star will help us assess the possibility of binarity, which could also explain the formation of its rare [WN] star and its nebular morphology.

ACKNOWLEDGEMENTS

A.D. wishes to express gratitude to Professor Quentin Parker and the staff at Siding Spring Observatory for supporting the Australian National University 2.3-m observation and the anonymous referee for constructive comments and thoughts.

DATA AVAILABILITY

The data underlying this article will be shared on reasonable request to the corresponding author. The 3D model is available on Sketchfab (<https://skfb.ly/o7nxA>), and archived on Zenodo (doi:10.5281/zenodo.5511247).

REFERENCES

- Abell G. O., 1955, *PASP*, **67**, 258
 Abell G. O., 1966, *ApJ*, **144**, 259
 Akas S., López J. A., 2012, *MNRAS*, **425**, 2197
 Akas S., Clyne N., Boumis P., Monteiro H., Gonçalves D. R., Redman M. P., Williams S., 2016, *MNRAS*, **457**, 3409
 Chambers K. C., et al., 2016, arXiv e-prints, p. arXiv:1612.05560
 Cignoni P., Callieri M., Corsini M., Dellepiane M., Ganovelli F., Ranzuglia G., 2008, in Eurographics Italian Chapter Conference. The Eurographics Association, pp 129–136, doi:10.2312/LocalChapterEvents/ItalChap/ItalianChapConf2008/129-136
 Danehkar A., 2015, *ApJ*, **815**, 35
 Danehkar A., 2021a, arXiv e-prints, p. arXiv:2107.03994
 Danehkar A., 2021b, *ApJS*, **257**, 58
 Danehkar A., Todt H., Ercolano B., Kniazev A. Y., 2014, *MNRAS*, **439**, 3605
 Danehkar A., Parker Q. A., Steffen W., 2016, *AJ*, **151**, 38
 Danehkar A., Karovska M., Maksym W. P., Montez Rodolfo J., 2018, *ApJ*, **852**, 87

- DePew K., Parker Q. A., Miszalski B., De Marco O., Frew D. J., Acker A., Kovacevic A. V., Sharp R. G., 2011, *MNRAS*, **414**, 2812
 Derlopa S., Akas S., Boumis P., Steffen W., 2019, *MNRAS*, **484**, 3746
 Dopita M. A., et al., 1996, *ApJ*, **460**, 320
 Dopita M., Hart J., McGregor P., Oates P., Bloxham G., Jones D., 2007, *Ap&SS*, **310**, 255
 Dopita M., et al., 2010, *Ap&SS*, **327**, 245
 Flewelling H. A., et al., 2020, *ApJS*, **251**, 7
 Frew D. J., et al., 2014, *MNRAS*, **440**, 1345
 García-Díaz M. T., López J. A., Steffen W., Richer M. G., 2012, *ApJ*, **761**, 172
 Gesicki K., Zijlstra A. A., 2000, *A&A*, **358**, 1058
 Jewitt D. C., Danielson G. E., Kupperman P. N., 1986, *ApJ*, **302**, 727
 Jones D., et al., 2010, *MNRAS*, **408**, 2312
 Jones D., Mitchell D. L., Lloyd M., Pollacco D., O’Brien T. J., Meaburn J., Vaytet N. M. H., 2012, *MNRAS*, **420**, 2271
 Kniazev A. Y., et al., 2008, *MNRAS*, **388**, 1667
 Kromov G. S., Kohoutek L., 1968, *Bull. Ast. Inst. Czech*, **19**, 1
 López J. A., García-Díaz M. T., Steffen W., Riesgo H., Richer M. G., 2012, *ApJ*, **750**, 131
 Miller Bertolami M. M., Althaus L. G., Olano C., Jiménez N., 2011, *MNRAS*, **415**, 1396
 Miszalski B., Crowther P. A., De Marco O., Köppen J., Moffat A. F. J., Acker A., Hillwig T. C., 2012, *MNRAS*, **423**, 934
 Mitchell D. L., Pollacco D., O’Brien T. J., Bryce M., López J. A., Meaburn J., Vaytet N. M. H., 2007, *MNRAS*, **374**, 1404
 Munoz M., Moffat A. F. J., Hill G. M., Shenar T., Richardson N. D., Pablo H., St-Louis N., Ramiamananantsoa T., 2017, *MNRAS*, **467**, 3105
 Parker Q. A., et al., 2005, *MNRAS*, **362**, 689
 Perek L., Kohoutek L., 1967, *Catalogue of Galactic Planetary Nebulae*. Publication House Czechoslovak Academy of Sciences: Prague
 Steffen W., López J. A., 2006, *RMxAA*, **42**, 99
 Steffen W., García-Segura G., Koning N., 2009, *ApJ*, **691**, 696
 Steffen W., Koning N., Wenger S., Morisset C., Magnor M., 2011, *IEEE Trans. Vis. Comput. Graphics*, **17**, 454
 Todt H., Peña M., Hamann W. R., Gräferer G., 2010, *A&A*, **515**, A83
 Todt H., et al., 2013, *MNRAS*, **430**, 2302
 Tyndall A. A., Jones D., Lloyd M., O’Brien T. J., Pollacco D., 2012, *MNRAS*, **422**, 1804
 Wachter S., Mauerhan J. C., Van Dyk S. D., Hoard D. W., Kafka S., Morris P. W., 2010, *AJ*, **139**, 2330
 Wareing C. J., Zijlstra A. A., O’Brien T. J., 2007, *MNRAS*, **382**, 1233
 Zijlstra A. A., Gesicki K., Walsh J. R., Péquignot D., van Hoof P. A. M., Minniti D., 2006, *MNRAS*, **369**, 875
 Zuckerman B., Aller L. H., 1986, *ApJ*, **301**, 772

This paper has been typeset from a \LaTeX file prepared by the author.